On the potential applications of acoustic emission in friction stir welding

Danilo Ambrosio, Gilles Dessein, Vincent Wagner, Malik Yahiaoui, Jean-yves Paris, Marina Fazzini, Olivier Cahuc

On the potential applications of acoustic emission in friction stir welding

D. Ambrosio [a,*], G. Dessein [a], V. Wagner [a], M. Yahiaoui [a], J.-Y. Paris [a], M. Fazzini [a], O. Cahuc [b]

[a] Laboratoire Génie de Production, Université de Toulouse, ENIT, 65016 Tarbes, France
[b] Institut de Mécanique et d'Ingénierie, Université de Bordeaux, CNRS, ENSAM, 351 cours de la Libération, Talence, France

ARTICLE INFO

Keywords:
Acoustic emission
Friction stir welding
Tool-workpiece interaction
Internal defects

ABSTRACT

In friction stir welding (FSW), only a few studies related to acoustic emission (AE) signals analysis have been conducted. In this work, the potential application of AEs in FSW is explored from a phenomenological and monitoring point of view. In static tests, with the tool only rotating without advancing, the information hidden behind AEs concerning the tool-workpiece interaction was investigated. Additionally, the sensors' positioning analysis is considered by comparing the signals' features obtained by placing the sensor on the welding plate or the support. Then in the second part, the effective capability of detecting internal defects during friction stir welding through AE signals monitoring is addressed. The experimental tests were performed on aluminum alloys of two different heat treatable families. Differences in the material plastic behavior depending on the aluminum alloys and the rotational speed were revealed by AEs features such as the amplitude and the absolute energy. In addition, internal defect occurrence was correlated with a shift in the signal centroid frequency. The results are auspicious for employing AE signals to deepen the tool-workpiece interaction and identify internal defects.

1. Introduction

Manufacturing processes monitoring through acoustic emission (AE) signals analysis has been widely employed in recent decades to discern phenomena related to tool-workpiece interactions and plastic deformation [1]. Based on its definition, "*Acoustic emission is the class of phenomena whereby transient elastic waves are generated by the rapid release of energy from a localized source or sources within a material, or the transient elastic waves(s) so generated*" [2], AE represents useful physical quantities for the comprehension of the manufacturing process. In the class of phenomena responsible for the release of energy, the most important are the interaction between the tool and the workpiece [3] as well as the deformation mechanisms [4]. For this reason, AE signals can reveal helpful information that can hardly be monitored during the processes [5]. However, the coupling of a particular AE signal to a specific physical phenomenon is not straightforward [6]. Therefore, a good knowledge of the process is essential to explain certain acoustic emissions trends. This type of monitoring has been applied to various manufacturing processes [7]. In friction stir welding, the potential of these signals has not yet been fully exploited.

Li et al. [8] gave a review on several applications of AE in turning. The authors explained the signals' features and why they have been applied in several manufacturing processes. First, AE signals are characterized in a frequency range higher than the machine vibrations and environmental noises. Then, the possible sources of AE in machining are the plastic deformation of the workpiece, plastic deformation of the chip, and frictional contact between the tool and the workpiece. Similarly, Jayakumar et al. [9] listed different applications of acoustic emission signals analysis focusing more on forming processes. The authors emphasized that in forming processes, acoustic emission characteristics are a function of various factors, including properties of the workpiece material, experimental conditions (strain rate and temperature), and elastic wave source (plastic deformation, fracture, friction, etc.). Among the principal information reported in the review, the possibility of monitoring the contact between the tool and the workpiece stands out. In sheet metal forming, information about the friction and the relative speed between the surfaces were correlated to the acoustic emissions. Additionally, in the forming processes, acoustic emissions helped to study the stick-slip phenomenon between the tool and workpiece. Behrens et al. [10] exploited the potential of AE signals for monitoring the occurrence of cracks in sheet metal forming. The authors highlighted the differences in signals amplitude depending on the processed material, showing the difficulties encountered by AE in detecting cracks when ductile materials were employed. In Table 1 the main application of AE to processes similar to friction stir welding is reported.

Given the summary presented in Table 1, the potential of acoustic

* Corresponding author.
E-mail address: dambrosi@enit.fr (D. Ambrosio).

https://doi.org/10.1016/j.jmapro.2022.01.012

Table 1
Acoustic emission applications to manufacturing processes.

Process	Information about	Reference
Machining	Tool-workpiece interaction	[8]
	Plastic deformation in the workpiece and chip	
Forming	Tool-workpiece interaction	[9]
	Occurrence of cracks	[10]

emission to investigate plastic deformation and tool-workpiece interaction for FSW is revealed. Specifically, the interest relies on the fact that in friction stir welding, the complex tool-workpiece contact and plastic deformation play a crucial role in the material flow and final joint quality. To date, very few works focusing on the application of acoustic emission on FSW have been proposed. Hence, the full potential of monitoring AE signals during friction stir welding has not yet been explored. The information obtained from AE signals can open up new paths of investigation and thus help advance the understanding of the process at the local level in the tool-workpiece interaction that is then responsible for everything that falls under the name of thermo-mechanical phenomena that govern the outcome of the process.

The first work was published by Chen et al. [11], and it focused on the possibility of detecting the occurrence of defects in FSW recording the AE signals. In their experiments, the authors first performed a test in standard butt configuration, and then in the second configuration, they machined the two abutting plates to have three notches along the welding line. The chosen welding configuration was previously proven to be suitable for ensuring sound welding. With this approach, they wanted to study eventual modification in the AE signal when the tool encountered the voids and compare it with those obtained from the sound weld. The authors highlighted differences in the signals suggesting possible employment of online monitoring through AE signals to detect defects in FSW. Zeng et al. [12] showed the effectiveness of AE signals to predict tool wear in FSW. The main feature highlighted by the authors was the decrease in the signal amplitude when the tool wear increased. The justification was found in the modification at the interface between the worn pin and the welding material. The evolution of AE signals with welding parameters was investigated by Soundararajan et al. [13]. The authors were interested in possible information found in the AE signals about tool-workpiece interaction and welding state. For this purpose, several tests were performed by modifying the welding parameters during the process. Various combinations of process parameters (welding speed, rotational speed, and plunge depth) were tested to obtain as much information as possible. The authors observed fluctuations in the power spectrum density (PSD) when modifying the rotational speed. An increase in the rotational speed (and the heat generation) led to an increase in PSD in the low-frequency range (100–170 kHz). For higher rotational speed values, when a drop in the flow stress is expected due to the maximum possible temperature, PSD amplifies in the high-frequency range (220–260 kHz) while decreasing in the low-frequency range. Additionally, the influence of the plunge depth on AE was observed, with the high-frequency range PSD disappearing when the tool shoulder lost contact with the workpiece. Recently, Subramaniam et al. [14] tried to find a correlation between the AE and tensile strength of FSW welds depending on the tool profiles. Also, Rajashekar et al. [15] developed a model to assess the quality and strength of friction stir welds employing AE signals together with machine vision.

Given the wide use of AE monitoring in various manufacturing processes comparable to friction stir welding, such as machining and forming, it makes sense to extend the analysis of acoustic emission signals to friction stir welding. As far as the authors are aware, few applications can be found in the literature, and thus the potential of acoustic emissions as applied to FSW has not yet been fully explored. Therefore, AE signals may help deepen the process complexity and discern phenomena that are not alternatively studied given the inaccessibility to the tool-workpiece contact. To determine the potential use of AE applied to FSW, a step-by-step study was performed to explore the ability to detect tool-workpiece contact modifications, the influence of the sensor's position, and the identification of signal features linked to the appearance of internal defects.

2. Material and methods

2.1. Material

The tests were performed on aluminum alloys (AA), 3 mm thick, 140 mm wide and 180 mm long, 6082-T6 and 7075-T6, which although both heat-treatable, have different solidus temperatures and plastic behaviors. Their mechanical and thermal properties at room temperature are listed in Table 2. The choice depended on their wide industrial applications [19] and their extensive uses in friction stir welding [20].

The H11 steel tool was characterized by a frustum shaped threaded pin, and the grooved shoulder is presented in Fig. 1b. Considering the shoulder structure, the contact with the workpiece results in two areas: the one with the surface highlighted between two red dotted circles and the one generated by the features highlighted with black dashed curves (Fig. 1b). A composite support system made of a mild steel backing plate in the center and aluminum was employed.

2.2. Experimental setup

The tests were performed on an adapted CNC lathe machine, Somab Genymab 900. Two experimental campaigns were carried out: the first campaign studied the tool-workpiece interaction and the influence of the sensor position on the recorded data, and the second campaign focused on the detection of internal defects during the process. A sketch illustrating the system is shown in Fig. 2a. In setup 1, one sensor was fixed on the support, while the other was fixed on the plate (Fig. 2b). The experimental campaign with setup 1 consisted of static and dynamic tests. The former are so-called because the tool stays in place while rotating for 15 s once the shoulder touches the workpiece, while the latter are traditional bead-on-plates tests. Static tests were performed to evaluate whether the sensors could detect changes in the tool-workpiece interaction. Holding the tool in place eliminates the cyclic interaction component between the material layer and the pin, whereas the local interaction between the tool and the very hot material remains. Additionally, it is possible to analyze the mark left by the tool after staying in place while obtaining information about acoustic emissions and machine spindle power. Instead, dynamic tests were performed to reproduce FSW conditions and compare signals obtained from the two sensors and evaluate their differences. In contrast, in setup 2 (Fig. 2c) with two sensors attached to the support, 70 mm long bead-on-plates varying rotational speeds were run and subsequently analyzed to assess their quality. All parameters used in the various tests are summarized in Table. 3.

The machine's output power was measured to evaluate the energy required for one tool rotation, study its evolution with the rotational speed and correlate it with acoustic emissions and joint surface quality in static tests. The joint quality was first analyzed externally with a Keyence VHX6000 microscope, while cross-sections were examined with optical microscopic observations (Olympus PMG3) after polishing

Table 2
Mechanical and thermal properties of AA6082-T6 [16,17] and AA7075-T6 [18]. Yield stress (Y), ultimate tensile strength (UTS), strain at break (ε_f), solidus temperature ($T_{solidus}$), specific heat (c), thermal conductivity (λ).

Alloy (AA)	Y (MPa)	UTS (MPa)	ε_f (%)	$T_{solidus}$ (°C)	c (J/kg K)	λ (W/m K)
6082-T6	260	310	7	580	900	180
7075-T6	469	538	8	535	960	130

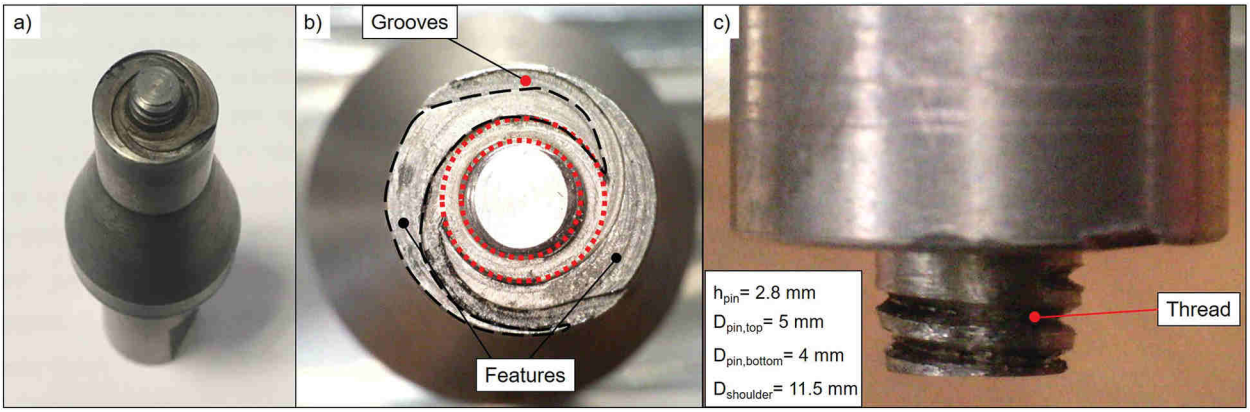

Fig. 1. FSW tool: a) 3D, b) top and c) front views.

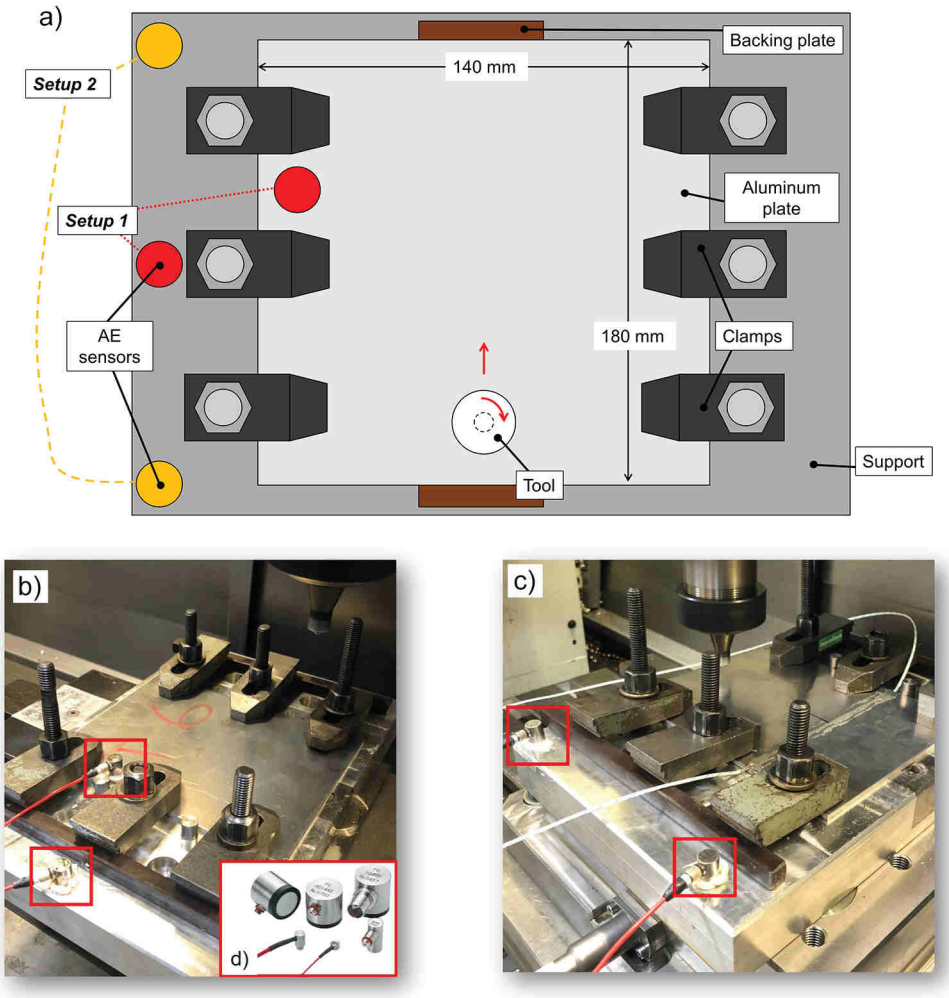

Fig. 2. View of the FSW experimental devices: a) sketch system, experimental configuration b) setup 1 and c) setup 2, d) AE sensors.

the specimens and then etching them with Keller reagent to reveal the microstructure.

2.3. Acoustic emissions

Piezoelectric sensors (Fig. 2d) allow recording the high-frequency energy signals generated during the process. The parameters used for the acquisition are listed in Table 4. These signals, in volts, are processed to form typical acoustic emission raw signals as shown in Fig. 3a. The type of burst and its characteristics are related to the process and its phenomenology [21]. Among the AE features, when analyzing the information collected with the sensors, the most relevant features were noted in the amplitude, absolute energy, and centroid frequency. The amplitude can be directly understood by looking at Fig. 3a, representing the highest peak of the burst. The absolute energy is always energetic information associated with elastic waves and is obtained by integrating

Table 3
Welding parameters for the two experimental campaign.

Setup	BM	v	N	BM	v	N
	AA	mm/min	rpm	AA	mm/min	rpm
1	6082-T6	Static	200	7075-T6	Static	200
			400			400
			600			600
			800			800
			1000			1000
			1200			1200
			1400			1400
			1600			1600
			1800			1800
			2000			2000
			2200			2200
			2400			2400
		180	1000		180	1000
2	6082-T6	180	500	7075-T6	180	500
			750			750
			1000			1000
			1250			1250
			1500			1500
			1750			1750
			2000			2000
			2250			2250

Table 4
Parameters for the acoustic emission acquisition. Peak definition time (PDT), hit definition time (HDT) and the hit lockout time (HLT).

Threshold (dB)	Preamplification (dB)	Sample rate (MHz)	Pre-trigger (µs)	PDT (µs)	HDT (µs)	HLT (µs)
30	40	10	50	200	800	1000

the squared voltage signal over the entire burst duration. It is given in atto-joule (aJ, 10^{-18} J) due to its small energy. The signal can also be transformed from the time domain to the frequency domain through the fast Fourier transform (FFT) to study the frequencies associated with the signal. The most interesting feature in the frequency domain is the centroid frequency, representing the center of mass of the AE signals and characterizing the overall frequency content (Fig. 3b).

The information gathered through the AE sensors allows us to focus on the phenomena related to tool-workpiece interactions. Frequencies associated with the dynamics of the FSW machine tool are less than 500 Hz, while the dynamical behavior is independent of the welding conditions (material and process parameters) [22].

2.4. Signal analysis

To better understand the static test, in Fig. 4a, we illustrate the plunging phase, the 15 s in which the tool remains in position rotating and then the retreating. During the tests, the machine spindle power and the torque derived from it were measured, and their evolution with time is shown in Fig. 4b. The power and torque after the initial transient associated with plunging stabilize over time. In the analysis, we focused on the torque to study the energy required as the rotational speed increases. Its mean value in the stable phase, i.e., in the second part of the test as shown by the red dashed rectangle in Fig. 4b, was calculated for all static tests.

Similarly, the considered AE features development over time during the static test is shown in Fig. 4c. They evolve stably during the process, thus we focused on their average values to compare their evolution with the rotational speeds.

The same applies to dynamic tests, where all the introduced quantities stabilize after the transient.

In all tests, the AE characteristics are calculated in the stable stage of the process (red dashed rectangle in Fig. 4c), corresponding to the stabilization of the machine's power signal obtained in the output. Therefore, the plunging, stabilization and retreating phases are never considered in the calculation of AE features.

3. Results and discussion

The results and discussion section is organized into several subsections to focus on the various issues. First, we focus on static test analysis primarily through observation of the traces left by the tool in correlation with energetic information to distinguish phenomenological features associated with the various rotational speeds employed. Then, we analyze the AE features to see if the previously observed transformations can be traced using this technique. We rely on the sensor fixed on the support that gives repeatable information in these two steps because it was never moved during the testing phase. Once we have proven AE features evolution with the associated phenomenologies, in the second part, we investigate the sensor position influence on the captured information to determine if it is possible to use a sensor fixed on the support without losing signal information. All experiments contained in this part were performed in setup 1. In addition, in the last part, we focus on practical cases to identify defects during bead-on-plate to reproduce FSW conditions using setup 2. Because the two sensors on the support provided the same information, only one was used for analysis.

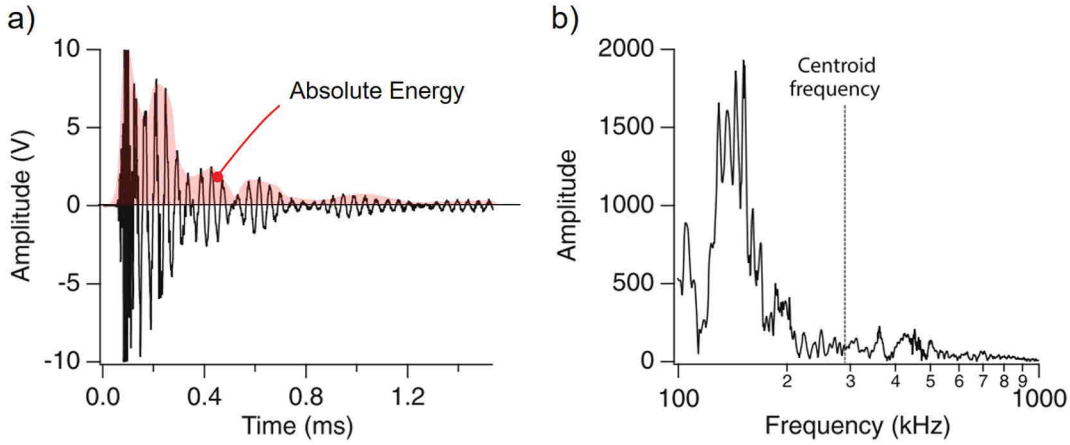

Fig. 3. Acoustic emission raw signal: a) temporal hit wave, b) FFT of a hit [21].

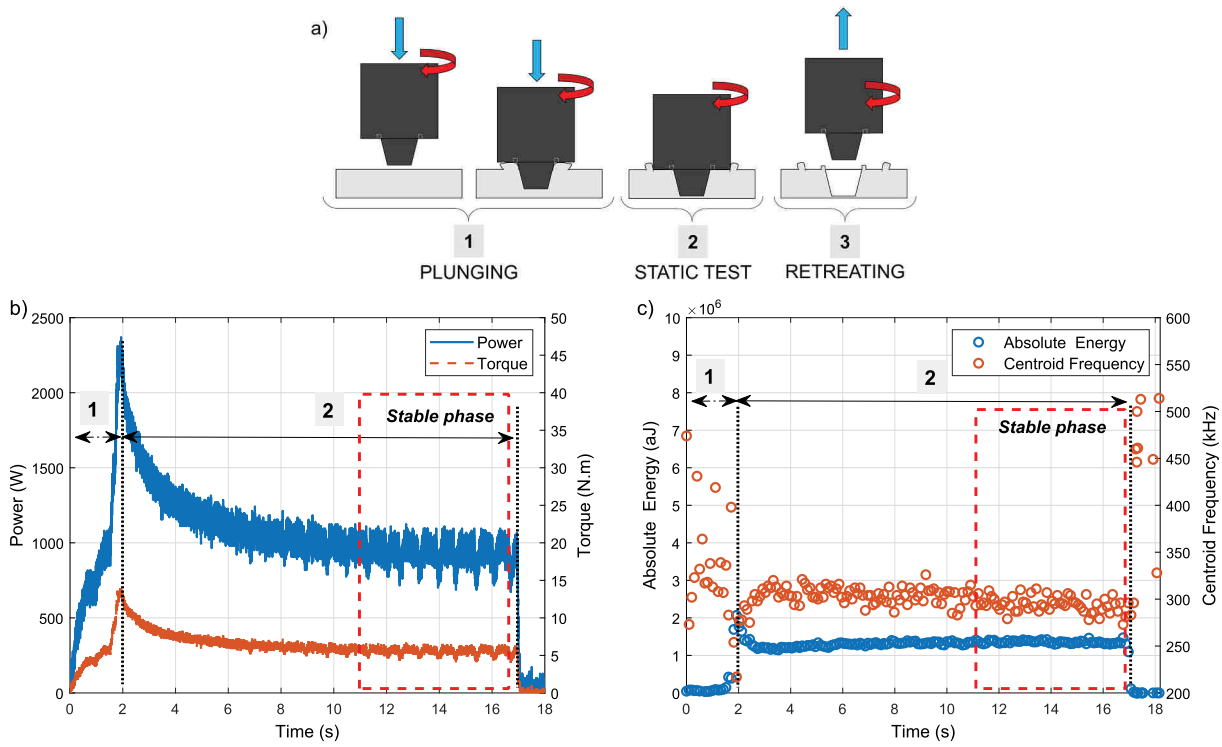

Fig. 4. a) Illustration of static test and acquired signals b) power and torque and c) absolute energy and centroid frequency. Configuration at 1200 rpm on AA6082-T6.

3.1. Detecting differences in tool-workpiece interactions

The static test analysis begins by studying the average energy evolution required in each test along with the geometric analysis of the trace left by the tool focusing on the exit hole diameter. For the energetic aspect, it is helpful to calculate the energy required for a rotation derived from the average power as follows:

$$M = \frac{P}{\omega}\left[\frac{\mathrm{J/s}}{\mathrm{rad/s}}\right] = E_{rad} = \left[\frac{\mathrm{J}}{\mathrm{rad}}\right] \tag{1}$$

$$E_{rot} = E_{rad}{}^{*}6.28319\left[\frac{\mathrm{J}}{\mathrm{rad}}\frac{\mathrm{rad}}{\mathrm{rot}}\right] = \left[\frac{\mathrm{J}}{\mathrm{rot}}\right] \tag{2}$$

where M is the torque, P is the spindle machine power and ω is the angular speed in radians per second. The torque can be interpreted as an energy per radian (E_{rad}), and multiplying it by the conversion factor from radian to 360° rotation, the energy per rotation (E_{rot}) can be obtained. The energy for one rotation is an indicator of the material's resistance to the tool action. Instead, the exit hole diameter left by the pin is calculated as shown in Fig. 5 for all tests.

The energy per rotation and exit hole diameter evolution as a function of rotational speed is shown in Fig. 6. Simultaneously, in the graphs, the difference between the energy for two consecutive configurations (i.e. $\Delta E_{1000} = E_{1000} - E_{800}$ energy for a rotation at 1000 rpm minus that at 800 rpm). The exit hole diameter evolution with rotational speed seems to be divided into three zones for both materials, as shown in Fig. 6a and b. It is approximately 4.9 and 5.2 mm at low rotational speeds. Subsequently, as the rotational speed increases, the exit hole diameter increases and stabilizes at approximately 5.4 mm and then decreases again by further increasing the rotational speed. The trend, although with some differences, is similar for both materials. The differences consist mainly of the transition thresholds. This development can be explained by analyzing the energy per rotation change with the rotational speed. It decreases dramatically in the first increments of rotational speed, but then the reduction slows down until it reaches a plateau. The evolution

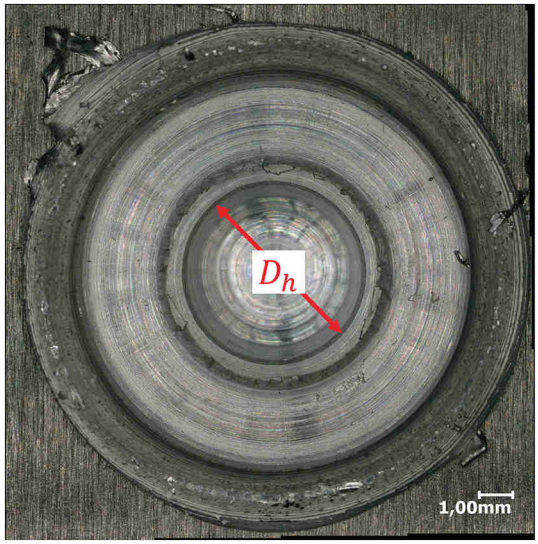

Fig. 5. Trace left by the tool and exit-hole.

suggests the initial material resistance, but the higher rotational speeds generate more heat, the temperature rises, and the workpiece strength collapses until stabilization is achieved at maximum softening. This trend is highlighted by observing the ΔE evolution, tending asymptotically to zero for the highest rotational speeds. The energy per rotation follows the three zones identified by observing the exit-hole diameter. Thus, one can explain this evolution as follows:

- In the first region, the rotational speeds are low, and the resulting heat generated and temperatures reached are not sufficient to lower the workpiece resistance requiring high energy to rotate with a

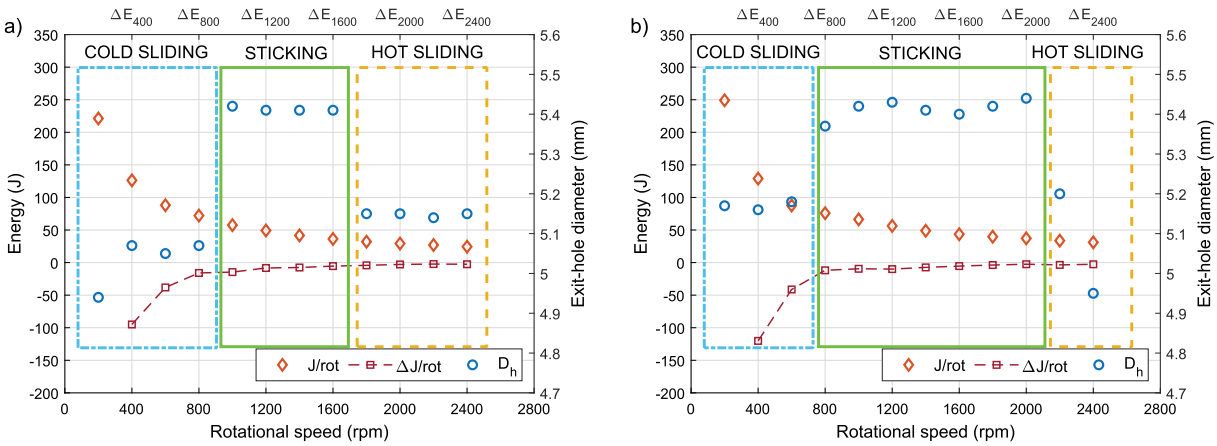

Fig. 6. Exit-hole diameter and energy for one rotation as function of the rotational speed: a) AA7075-T6 and b) AA6082-T6.

consequent smaller diameter due to a mainly sliding contact between the tool and workpiece. This region can be referred to as *cold sliding*.

- Instead, the energy stabilizes in the second zone, reaching the larger exit hole diameter. This result is justified by achieving the maximum material softening caused by pronounced aluminum sticking around the pin explaining the larger output diameter. The zone corresponding to intermediate rotational speeds can be defined as *sticking*.
- Finally, in the last zone, the energy reaches a plateau, and it is evident by observing the differential that tends to zero asymptotically while the exit hole diameter decreases again. This result can be explained by the attainment of maximum softening, vanishing the rotational speed effect on the material resistance. Moreover, the plastic deformation localization caused by the increase in shearing rate could induce local incipient melting phenomena justifying a new sliding between the tool and workpiece and decreasing the exit hole diameter. Hence, the high rotational speed region can be referred to as *hot sliding*.

According to Fig. 6, the cold sliding-sticking transition occurs at 800–1000 rpm for AA7075-T6 and at 600–800 rpm for AA6082-T6, while the transition from sticking zone to hot sliding occurs at 1600–1800 rpm and 2000–2200 rpm for AA7075-T6 and AA6082-T6, respectively. Clearly, during FSW, the tool-workpiece interaction is always a mixed condition between sliding and sticking [23]. Then, the areas designated as sliding and sticking indicate a region where one component prevails over the other; low and high rotational speeds lead to more sliding than sticking, while in the intermediate regime, sticking is maximized. The classification is made to facilitate subsequent analysis.

To study the differences obtained in the various static tests, the traces left by the tool after the retreating were observed. All marks on both

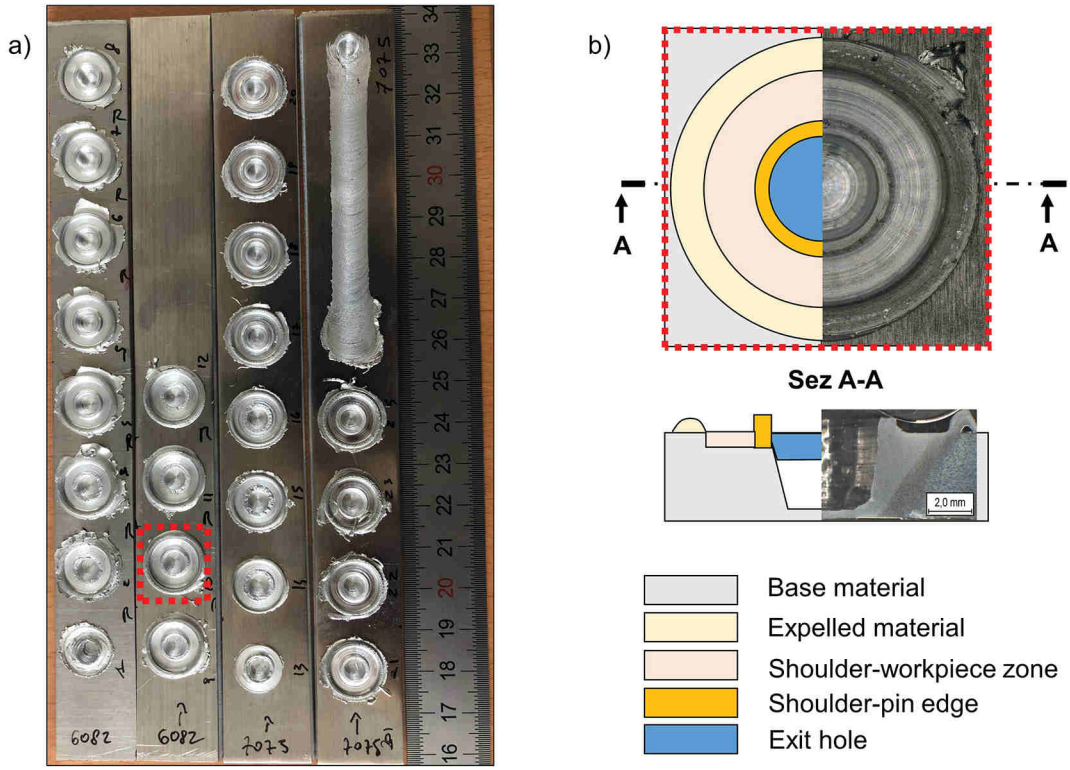

Fig. 7. Static tests: a) marks left by the tool, b) scheme of the different zones composing the mark.

materials are shown in Fig. 7a. From the analysis of the surfaces, it is possible to divide the trace left by the tool into various parts:

- the first one, the most external, represents the material expelled by the tool during the plunging until the complete contact of the shoulder with the workpiece;
- then, going inwards, there is the shoulder-workpiece contact zone;
- between the shoulder-workpiece contact zone and the exit-hole a third zone appears and represents, the shoulder-pin edge zone;
- in the inner part, there is the exit hole left by the pin.

The zones are schematically illustrated in Fig. 7b. Looking at the shoulder-pin edge zone, a triple transition can be observed in both materials (Fig. 8). Analyzing this area is particularly interesting because it represents the hotter zone during the process [17] with the higher tool pressure on the material, which is subject to the influence of both the pin and the shoulder. In addition, the shoulder shape highlighted in Fig. 1b by the red dotted circles explains the appearance of the shoulder-pin edge zone. Most of the surface interacts with the workpiece with both shoulder parts, i.e. grooves and features. In contrast, in the crown immediately after the pin, the shoulder-workpiece contact is homogeneous and free from shoulder features. Hence, it is easier to focus on this contact zone because the tool-workpiece interaction is simpler.

The zones were classified into three surface types by observing the shoulder-pin edge zone. The first, at low rotational speeds, Fig. 8a and d, shows an irregular surface both in the rotation direction and perpendicular to it. This type of surface seems to result from severe adhesive phenomena, i.e. the shoulder tries to drag the material with it, but it cannot deform continuously, generating an irregular fragmented surface. The phenomena consist of a stick-slip contact [24] with the shoulder discontinuously dragging the workpiece generating the irregular surface shown in Fig. 8d. The texture changes entirely by increasing the rotational speed, showing scratches in the rotation direction (Fig. 8b and e). In this case, it seems that at the shoulder-workpiece, interface abrasive phenomena occur. The harder material (tool) scratches the softer (workpiece) during the relative motion generating the scratched surface. A further increase in rotational speed determines the last surface transformation, as shown in Fig. 8c and f, which again appears irregular. Adhesive phenomena take over entering warmer regimes associated with high rotational speeds. The stick-slip phenomenology seems distributed over the entire surface as if the alternating contact varies significantly on the whole surface, with material missing locally. The transition from one type of surface to another follows the same rotational speed thresholds identified earlier in the definition of cold sliding, sticking and hot sliding zones. The insufficiently high temperatures obtained at low rotational speeds mean less ductile workpieces and difficulties in plastic deformation. The consequence is adhesive phenomena generating irregular fractured surfaces (cold sliding → cold adhesive phenomena). Then, the higher temperatures increase the workpiece softening within the sticking zone, and the shoulder surface can continuously deform the material. Because there is always a relative movement between the tool and workpiece, abrasive phenomena occur, as proven by the scratched surfaces in the rotation direction (sticking → abrasive phenomena). Finally, when the maximum softening has already been reached, a further increase in rotational speed generates temperature increases induced by localized plastic deformation. The additional temperature rise causes incipient local melting disturbing the contact, and the appearance of surfaces suggests new high-temperature adhesive phenomena with discontinuous deformation due to incipient local melting (hot sliding → hot adhesive phenomena). The transitions and various surfaces are shown schematically in Fig. 9 to summarize the results. According to the energy per rotation evolution, different cohesive and interfacial mechanisms justify the differences observed in the surfaces.

To further understand what is occurring at the tool-workpiece interface, it is helpful to analyze the cross-sections of some configurations. For both materials, samples obtained at 1000 and 2400 rpm were studied. The configurations were chosen because the 1000 rpm configuration falls within the sticking zone, with the maximum exit-hole diameter, while the 2400 rpm configuration represents the hot sliding zone with the onset of local incipient melting. Fig. 10a and b display the cross-sections for AA7075-T6 at 1000 and 2400 rpm.

Two things are worth noting when analyzing the 7075 specimens. First, the nugget zone (NZ) width does not significantly change between the two configurations, with its width measured at the mid-thickness, as shown in Fig. 10 equal to 7.5 and 7.4 mm, for 1000 and 2400 rpm,

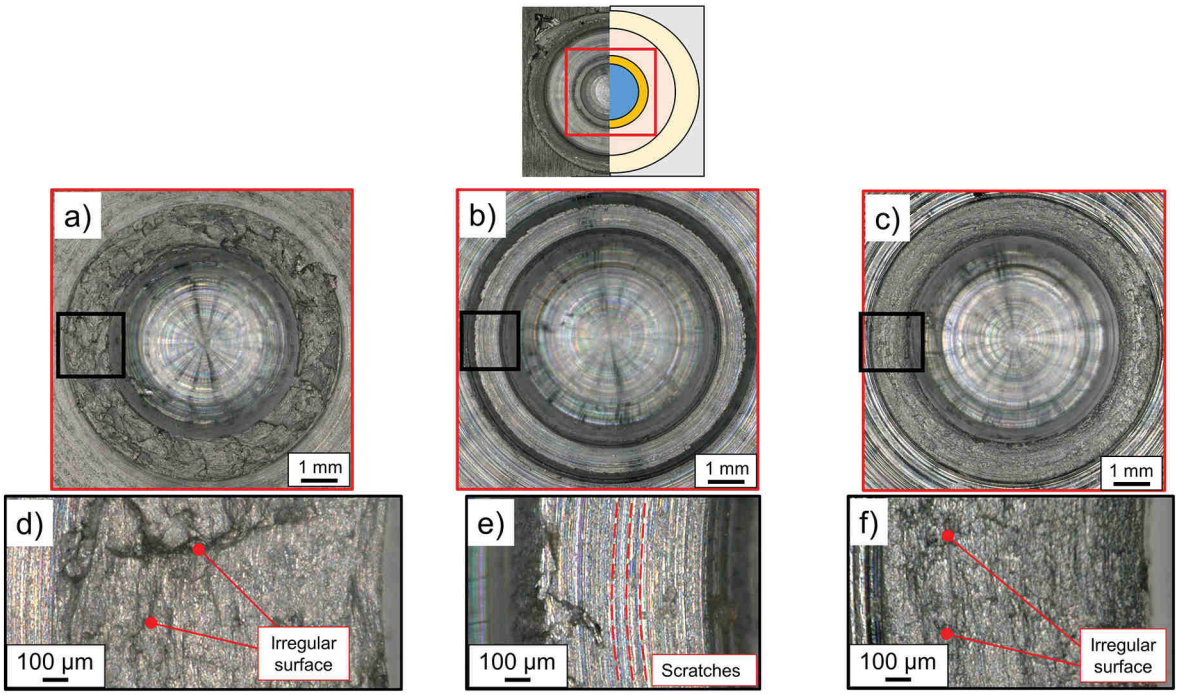

Fig. 8. Triple transition obtained in static tests on AA7075-T6: a) and d) 400 rpm, b) and e) 1200 rpm, c) and f) 2400 rpm.

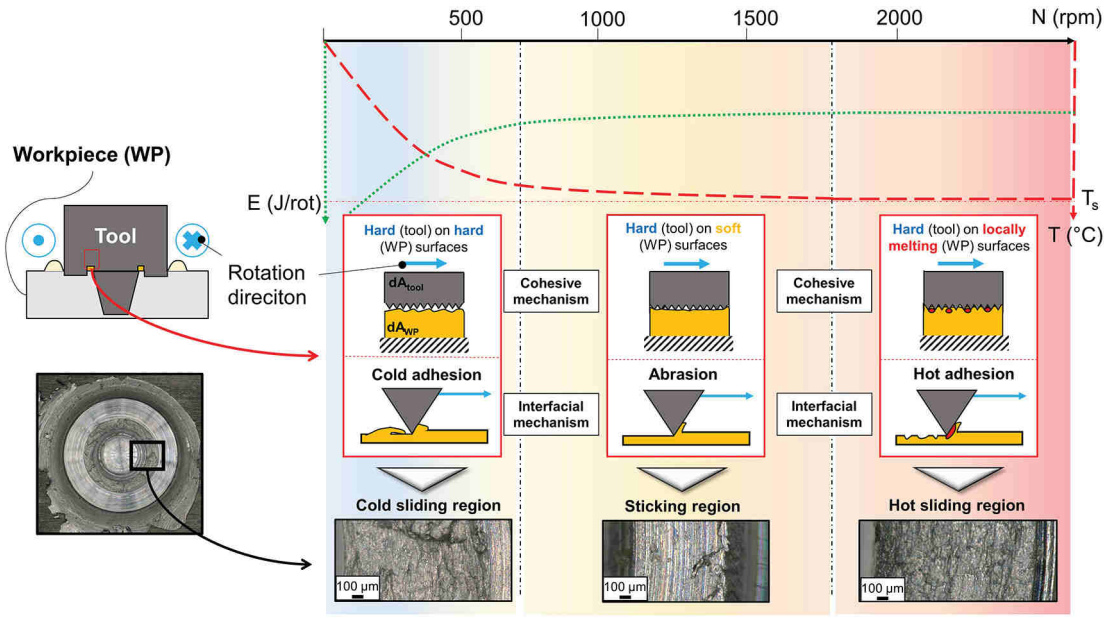

Fig. 9. Shoulder-pin edge zones modifications according to various contact phenomena induced increasing the rotational speed.

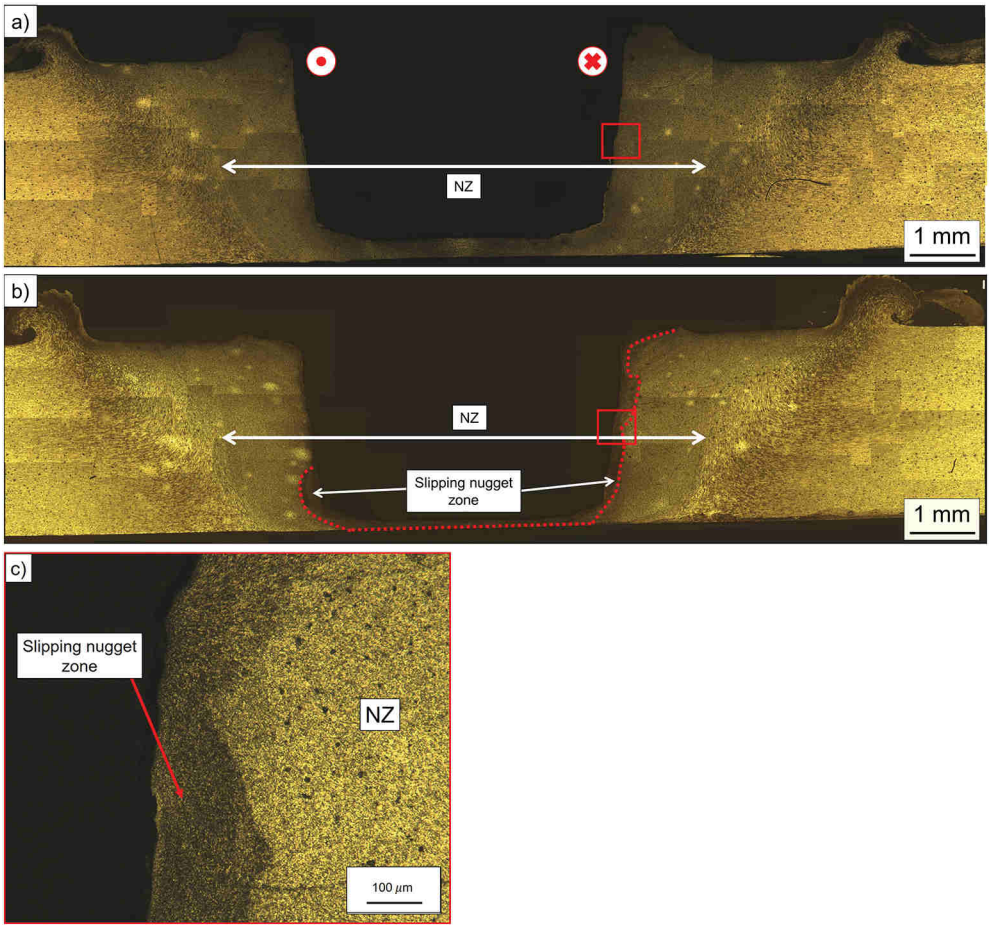

Fig. 10. Cross-section of AA7075-T6 samples: a) 1000 rpm, b) 2400 rpm, c) magnification on the slipping nugget zone.

respectively. The second is the appearance of a third zone in the 2400 rpm configuration. The processed material directly in contact with the tool seems to differ from the nugget zone by presenting a different response to etching. Its magnification is shown in Fig. 10c, referred to as the slipping nugget zone. A closer analysis to assess differences in microstructure around the pin in the two samples was done in the zone highlighted by the two red squares in Fig. 10a and b. By comparing Fig. 11a and b, the difference between the two microstructures can be

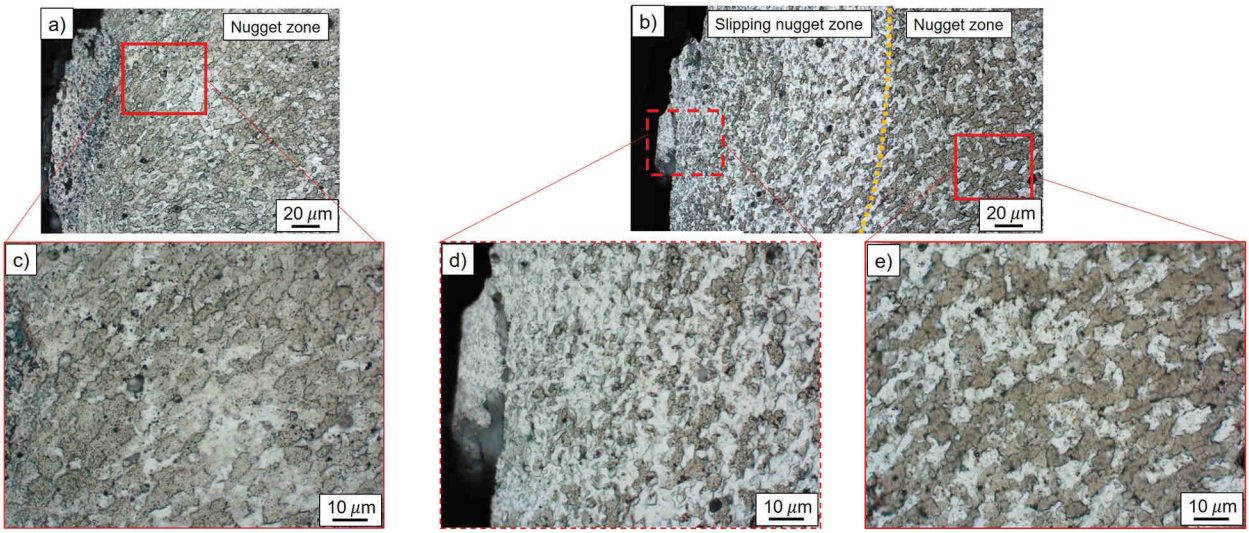

Fig. 11. Closer microstructures observations at the contact interface between the periphery of the rotating tool and adjacent material.

detected, with a single zone (i.e., nugget zone) in Fig. 11a and two zones in Fig. 11b (i.e., slipping nugget and nugget zones) responsible for the different etching shown in Fig. 10c.

This microstructural modification helps to understand the reduction in exit hole diameter discussed above. In an intermediate range of rotational speeds, maximum sticking is achieved with an aluminum

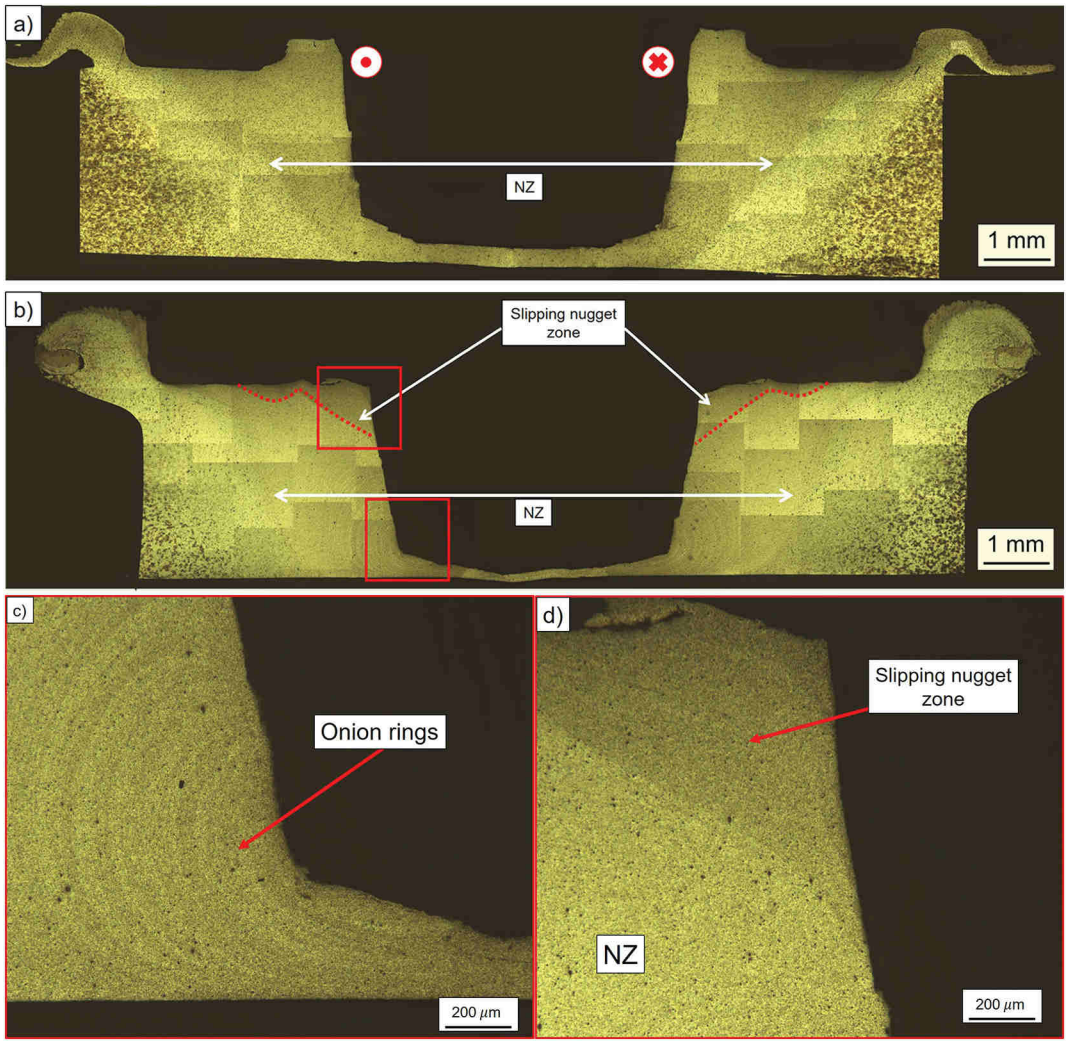

Fig. 12. Cross-section of AA6082-T6 samples: a) 1000 rpm, b) 2400 rpm, c) magnification of the onion ring structure, d) magnification on the slipping nugget zone.

layer being carried away by the tool during retreating with a resulting larger exit hole diameter and higher rotational rates result in a different increase in sliding induced by local incipient melting. The consequence is a decrease in the sticking between the pin lateral surface and the sheared material. Then during the retreating phase, the layer previously stuck to the pin can be found in the microstructure analysis represented by the slipping nugget zone (Fig. 11d). This result is corroborated by Gerlich et al. [25], proving the transient local melting and tool slippage at the contact interface between the periphery of the rotating tool and adjacent material in the stir zone during friction stir spot welding AA7075-T6 at high rotational speeds when the solidus temperature is exceeded. Therefore, the transition zones identified through the exit hole diameter evolution indirectly confirms the increased slipping at higher rotational speed due to local incipient melting at the tool-workpiece interface, and microstructural observations in Fig. 11 corroborate it. Cross-sections of AA6082-T6 samples are shown in Fig. 12a and b. The first thing to note is the overall change in NZ by comparing the two samples. The nugget zone width, measured at the mid-thickness, changes from 7.8 to 8.4 mm. Additionally, surprisingly, one can see the onion ring structures (Fig. 12c) in the test at 2400 rpm, likely justified by the viscous material behavior. Under this condition, the sheared material is pushed down by the pin thread action generating the onion ring structure just as happens during FSW [26]. Also, in this case, in the configuration at 2400 rpm, a third zone appears (Fig. 12d), this time localized only in the shoulder-pin edge zone that can be explained again as a possible zone in which the material has exceeded its solidus temperature with the consequent increase in tool slippage.

Finally, the last characteristic common to the two materials and confirming the differences in the shoulder-pin edge zone is shown in Fig. 13. By comparing the cross-sections obtained at 1000 and 2400 rpm for AA6082-T6, observing the tool profile depicted in black dashed lines, it is noted that there is a missing part highlighted by the dashed red circles in the hottest configuration. The outcome may be explained in two ways: either this portion of the material in these thermomechanical conditions becomes attached to the tool and then the contact in the area becomes aluminum-aluminum and not steel-aluminum, or even if there is still a relative movement between the tool and workpiece while rotating, during the retreating, the material melted locally given the temperatures reached remains stuck in the groove thus determining the material removal. Regardless of the explanation, this confirms the previous hypothesis about hot sliding conditions due to local incipient melting in the hottest area in the corner between pin and shoulder [17].

Hence, the cross-sectional analysis confirmed the changes in the tool-workpiece contact in the investigated rotational speed ranges.

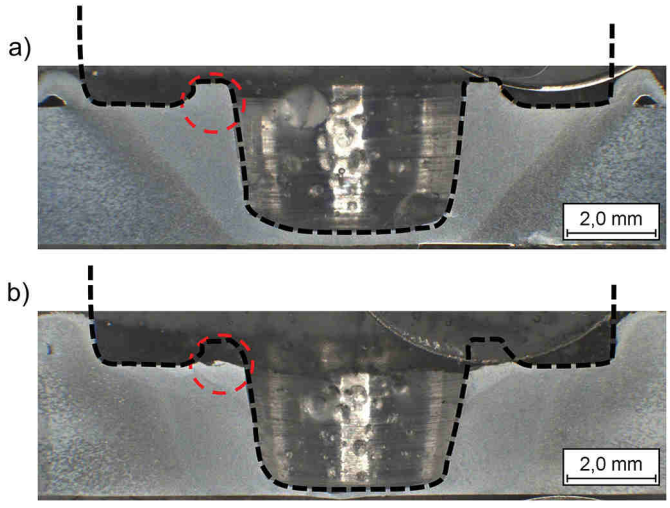

Fig. 13. Shoulder-pin edge zones analysis from AA6082-T6 cross-sections view: a) 1000 rpm, b) 2400 rpm.

3.2. AE analysis

The information gathered by observing the trace left by the tool, the energy per rotation and microstructural observations allowed the identification of different tool-workpiece interactions associated with the material softening state. The goal is to see if it is possible to trace these changes related to local transformations through the AE analysis obtained from the sensor on the support. Fig. 14 shows the evolution of the centroid frequency and absolute energy. Starting from the frequency analysis, it can be observed that this is independent of the rotational speed or does not directly correlate with the latter. Additionally, it is worth pointing out the different frequency ranges when comparing the two materials. Without considering the 200 rpm configuration, it is possible to identify centroid frequencies between 250 and 300 kHz for AA7075-T6 and 300 and 350 kHz for AA6082-T6. The fact that these are different suggests that the phenomena generating the elastic waves in static tests are diverse. In other words, the combination of mechanical phenomena (i.e., plastic deformation and tool-workpiece friction) and thermal phenomena (softening and microstructural transformations) are different for the two materials when the tool is not advancing. This result is not trivial because it shows substantial differences between the two materials, which are inevitably reflected during welding, resulting in different weldability. In addition, as far as absolute energy is concerned, this seems to be more directly related to the rotational speed with a more or less continuous increase with rotational speed.

Focusing instead on their evolution with the rotational speed rather than comparing the two materials, transitions, as already observed qualitatively by analyzing the surfaces of the tool traces and the energy for one rotation can be detected. For AA7075-T6, based on previous observations, the transition from a predominantly sliding contact to a sticking contact manifests itself with a continuous decrease in the centroid frequency. However, entering the sticking zone, the subsequent increase in rotational speed corresponds to the centroid frequency increase and then decreases again. Sliding then definitively takes over, where the sudden sticking drops due to local incipient melting of the secondary phases that complicate the contact with the pin (hot sliding). The interaction change is revealed by a new increase in centroid frequency from 1800 to 2400 rpm.

This phenomenological explanation also allows reasoning about the absolute energy evolution. In the beginning, it increases with the rotational speed in the cold sliding and sticking zones. Then, it stabilizes when frictional heat generation reaches saturation, attaining the maximum material softening around the tool. A further rotational speed increase determines the beginning of the alternating stick-slip condition due to the local melting of the secondary phases resulting in different energy releases during the tests at a rotational speed higher than 1600 rpm and causing a sudden rise in the standard deviation. The alternating stick-slip condition was proved by cross-section analysis pointing out the appearance of a third thin zone in the inner part of the NZ (Fig. 10c) and the reduction in the exit-hole diameter. The same assumptions can be extended for AA6082-T6. The centroid frequency continuously and gradually decreases in the first two zones, up to its minimum reached at 1600 rpm, and then increases again entering the hot sliding zone, although much less markedly than observed for AA7075-T6. The same is true for the absolute energy that grows with an exponential trend in the first two zones up to 1800–2000 rpm and then changes its evolution, increasing slowly without showing the same markedly higher standard deviation for the highest rotational speeds. In the hot sliding zone, the AA6082-T6 phenomenology is not very different from sticking, as confirmed by the cross-sections in Fig. 12, with the appearance of the third zone at 2400 rpm only locally in the shoulder-pin area and not along the entire pin contact surface. The stable and extended transition zone is justified by the excellent flowability of this aluminum alloy [27] and thus a more homogeneous behavior over a wider window of rotational speed. In addition, the absence of a sudden increase in the absolute energy standard deviation lies in the solidus temperature being

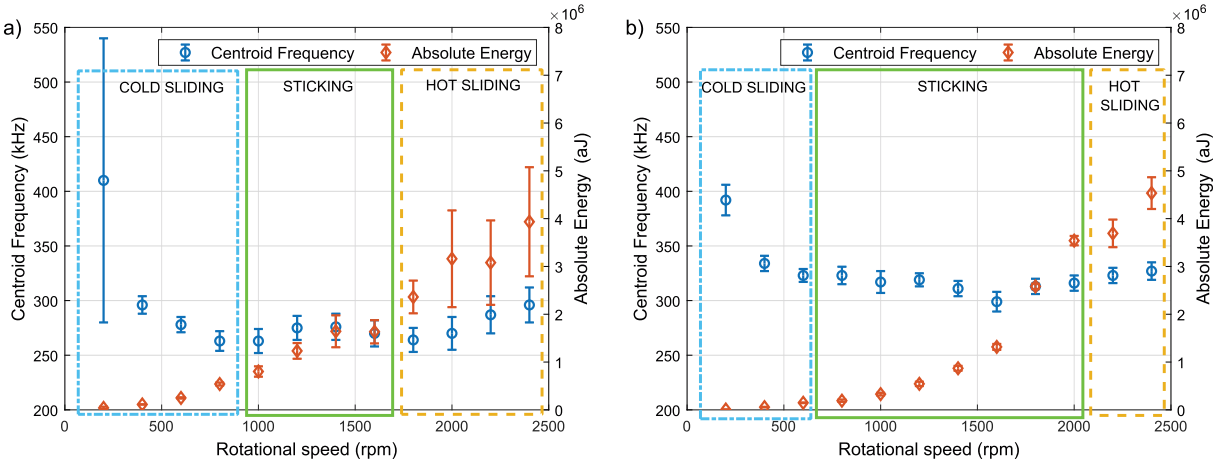

Fig. 14. Evolution of centroid frequency and absolute energy: a) AA7075-T6 and b) AA6082-T6.

much more complex to reach both because it is higher (580 °C vs. 535 °C of AA7075-T6) and because the thermal conductivity is higher (at room temperature 180 vs. 130 W/m K). This hypothesis is supported by the cross-section of the sample at 2400 rpm, where the third zone appears but only locally in the shoulder-pin edge zone and does not extend along the pin contact zone, as for AA7075-T6.

Thus, the two selected features can reveal changes in the tool-workpiece interaction depending on the thermal and mechanical regime governed in this type of test only by the rotational speed.

3.3. Influence of the sensor position on the information hidden behind the elastic waves

Sensor placement is an issue in acoustic emission applications in manufacturing processes [28]. In the case of FSW, it is necessary to understand eventual differences in fixing the sensor to the welding plate or the support on which the plate is clamped. This information is not essential from the research point of view because fixing the sensor on the plate between tests, although laborious, does not present difficulties. In contrast, from the point of view of in-situ monitoring of weld quality, it is essential to rely on a sensor fixed on the support, avoiding the sensor's relocation between tests. The problem is addressed by comparing the average value of the amplitudes and centroid frequencies recorded by the sensors on the welding plate and the support in all static tests. In addition, tests in a bead-on-plate configuration at 1000 rpm were performed to compare AE features including phenomena linked to the tool feed and cyclical pin-workpiece interactions.

From an energetic point of view, the amplitudes were analyzed. Fig. 15 displays the comparison between the amplitudes recorded by the two sensors for both aluminum alloys. The evolutions seem similar, with the amplitude increasing with the rotational speed. However, one must remember that amplitudes are expressed in decibels, and therefore even minor differences can represent a significant loss of information. A more representative quantity can be a loss coefficient between one sensor and another. This type of solution is typically used to evaluate the attenuation of elastic waves during propagation in the same structure by placing sensors at different distances from the source of acoustic emissions [29]. The coefficient can be calculated as:

$$\alpha = \frac{20}{D}\, log_{10}\frac{A_1}{A_2}\ [\mathrm{dB/m}] \tag{3}$$

A_1 and A_2 are the amplitudes recorded by the sensors, and D is their distance. In our case, because the sensors are not particularly distant but positioned on two different structures, it makes more sense to calculate the absolute attenuation, regardless of their distance (~30 mm). Therefore applying the same Eq. (3) but removing the distance, we can obtain the attenuation between the two sensors:

$$\alpha_n = 20\, log_{10}\frac{A_s}{A_p}\ [\mathrm{dB}] \tag{4}$$

A_s and A_p are the support and plate amplitudes, respectively. The absolute loss coefficient evolution as a function of the rotational speed

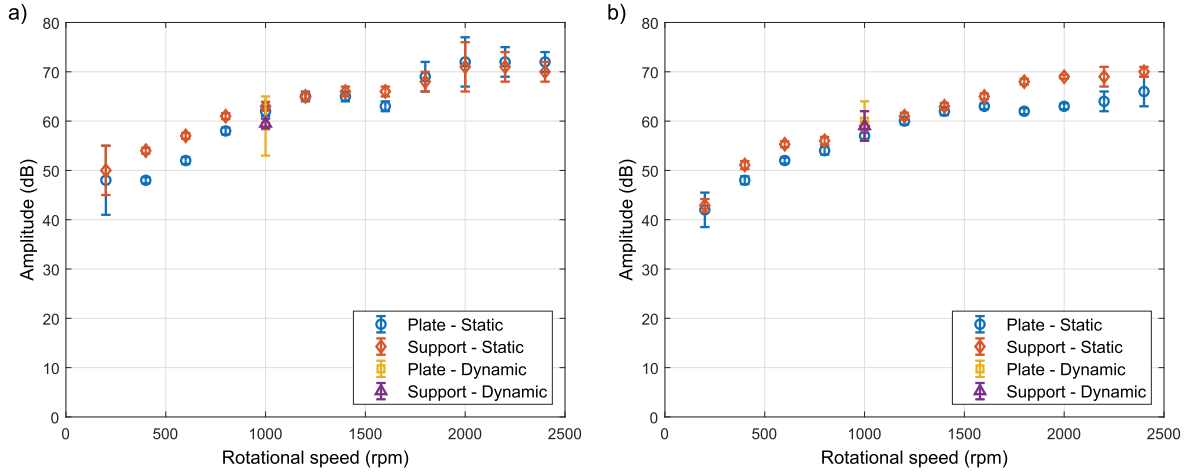

Fig. 15. Evolution of amplitudes as a function of the rotational speed: a) AA7075-T6 and b) AA6082-T6.

for the static and dynamic tests is shown in Fig. 16a. When α_n is positive, the sensor's amplitude on the support is greater, while if negative, A_p is higher than A_s. Analyzing the evolution of the parameter in the case of static tests on AA6082-T6, it can be observed that the evolution is more or less stable up to 1800 rpm, where a drastic increase in the coefficient appears, revealing the significant signal attenuation in the sensor fixed on the plate. This result is surprising because higher values were expected on the plate, i.e., where the source of these acoustic emissions is located. However, looking at the representation in Fig. 16b, it is possible to observe that around the tool, NZ represents an area that is mechanically and thermally affected by the tool rotation forming a new viscous medium between the source and the sensor fixed on the plate.

The damping of elastic waves when propagating in viscous media has previously been demonstrated [30]. In the AA6082-T6 cross-sections, going from 1000 to 2400 rpm, both an 8% NZ increase and a change in shape were observed with the appearance of the onion ring structure justified by the viscosity of the material processed by the tool. It is evident then how this leads to an attenuation of the elastic waves picked up by the sensor on the plate, contrary to those picked up by the sensor on the support that does not pass through this thick viscous material layer. For AA7075-T6, the evolution is more chaotic and remains in line with the analysis made in the previous section. In this case, it appears that the greatest attenuation of elastic waves by the viscous material around the tool occurs at lower rotational speeds. In contrast, at higher rotational speeds with hot sliding, it seems as if this effect vanishes, providing a greater amplitude in the waves recorded by the sensor on the plate. To look for an explanation, one must remember that softened material in FSW is considered as a non-Newtonian fluid with its viscosity depending on both temperature and shearing rate [31]. In the case of AA7075-T6, for the combination of temperature and shearing rate obtained at a high rotational speed, the viscosity of the medium is such that it does not attenuate the elastic waves. In general, it has already been shown that AA6xxx exhibits higher viscosities than AA7xxx at the same temperature and shearing rate [32], supporting what has been seen for the high rotational speed tests for AA6082-T6. In any case, what is important are the dynamic tests, which are the ones that are representative of FSW tests and then the ones used to evaluate the possible presence of defects. In the dynamic case, for both materials, A_p is greater than A_s. This result is caused by the tool feed and the consequent sharper thermal gradient. Hence, the viscous zone is significantly reduced, inducing higher amplitudes always detected on the plate, where the sources of the elastic waves are located. The comparison of the NZ of cross-sections obtained at 1000 rpm in static and dynamic tests is shown in Fig. 17. However, the differences are minor, and the energetic losses related to positioning do not seem to be a problem.

To complete the analysis on the influence of the sensor's position, centroid frequencies for the two sensors as a function of the rotational speed are depicted in Fig. 18. It is surprising and worth discussing the consistent gap found in the static tests on AA6082-T6. This difference is between 50 and 80 kHz. The same happens for AA7075-T6 but only at low rotational speeds (i.e., 400 and 600 rpm). The gap observed in the frequency content of the signals collected is not easy to explain. The hypothesis supported by the author is attributed to a specific material plastic behavior. In static tests, the material layer is continuously

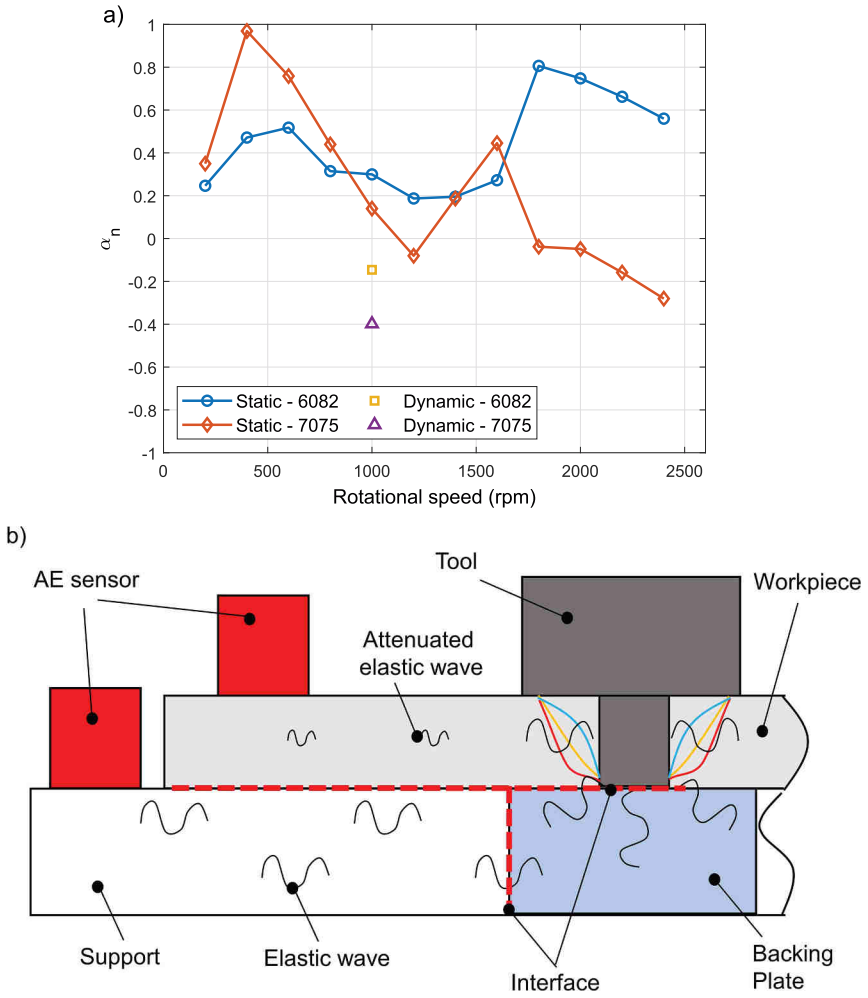

Fig. 16. a) Evolution of the absolute loss coefficient α_n as a function of the rotational speed, b) schematic representation of AE sensors positions.

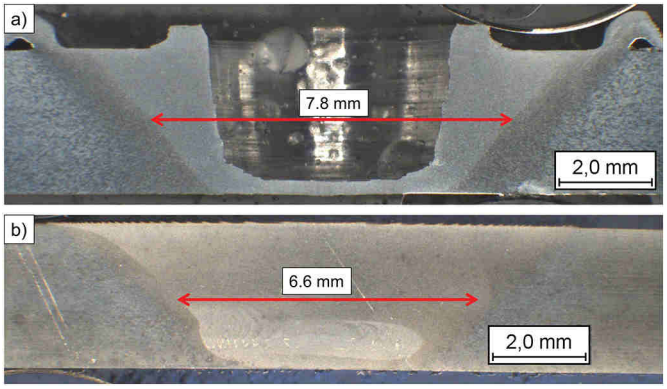

Fig. 17. AA6082-T6 cross-sections obtained at 1000 rpm for a) static and b) dynamic tests.

sheared by the tool. The way it reacts to the tool action depends on its plastic behavior under specific thermomechanical conditions. In a general sense, it is known that AA6xxx alloys are more ductile than AA7xxx at high temperatures, withstanding more plastic deformation before a fracture occurs [33]. Therefore, it can be assumed that for AA6082-T6, the material is continuously processed without the appearance of continuous fractures during shearing. The same may be true in a particular temperature and shearing rate range for AA7075-T6, whereas for higher rotational speeds, the layer is continuously fractured during tool rotation. The different phenomenology may be responsible for the shift in the signal frequency content recorded by the two sensors, with a higher centroid frequency for the sensor placed on the plate. The proposed hypothesis cannot be confirmed in this work, as it would require fine rheological analysis of the two materials in particularly severe thermomechanical regimes. Thus, it can be thought of as one of several perspectives of this study related to the investigation of tool-workpiece contact through acoustic emissions. However, it is important to observe the closeness of the frequency contents registered by both sensors in the dynamic tests (Fig. 18). Additionally, they look like the values recorded in the static tests by the sensors on the support. This result may partially confirm the abovementioned hypothesis. In the FSW tests, the cyclicity is intrinsic to the process with the layer processed and then released as the tool advances, thus losing the effect of continuous deformation of a layer mentioned earlier to explain the frequency differences.

In conclusion, the comparison between the information collected by the two sensors revealed differences attributable to the process phenomenology and the viscosity of the material around the tool. Additionally, regarding positioning, it was found that the sensor can be safely placed on the support. The comparisons obtained in the dynamic tests confirmed the similar information obtained in terms of energy and frequency.

3.4. *Relationship between internal defects and AE*

After highlighting the potential for acoustic emission, a wide window of rotational speed is investigated on both materials by running bead-on-plate at a welding speed of 180 mm/min and varying the rotational speed from 500 to 2250 rpm. Based on the information gathered above, all the welds' centroid frequencies and absolute energies were analyzed.

The weld quality, centroid frequencies and absolute energies as a function of the rotational speeds are shown in Fig. 19a and b for AA7075-T6 and AA6082-T6, respectively. The evolution of the absolute energy follows the same trend observed in the static tests. First, it suddenly increases with the rotational speed in the low range, passing through a period of stabilization and then starting to grow again abruptly for the highest rotational speed values, approximately beyond 1500 rpm.

Centroid frequencies are within 230–280 kHz for the tests on AA7075-T6. However, the first configuration at 500 rpm, the only one corresponding to the sound joint obtained on this material, corresponds to an average centroid frequency of 272 kHz. All the others, corresponding to internal and external defects, are characterized by frequencies that first decrease and then increase at higher rotational speed values but consistently below 250 kHz. In particular, the joints characterized by internal defects present the lowest centroid frequencies. Fig. 20 takes the earlier split into zones made according to tool-workpiece interactions showing the weld quality and absolute energy evolution as a function of rotational speeds.

For AA6082-T6, the weldability is higher, with defect-free joints obtained from 1000 rpm onward. The first test at 500 rpm provided a cold joint characterized by an apparent surface defect, and a centroid frequency over 300 kHz distinguished this configuration. Subsequently, when gradually increasing the rotational speed, the joints at 750 and 1000 rpm presented microvoids located between consecutive layers and onion ring area not thoroughly developed, the symptom of a maximal softening not yet reached, and then from 1500 rpm onwards with the typical onion ring shape and without problems associated with too high rotational speeds. The surface defect, microvoids and cross-sections of healthy joints as a function of rotational speed are shown in Fig. 21. All configurations were characterized by rotational speed higher than 500 rpm and showed an average centroid frequency above 250 kHz. AE signals were unable to detect the cold internal microvoids obtained at

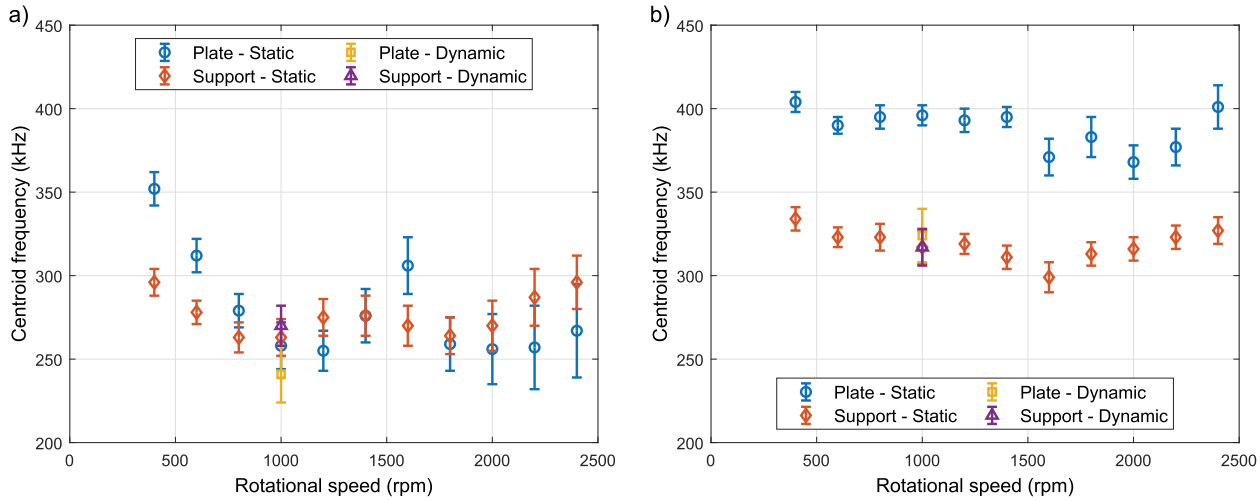

Fig. 18. Evolution of centroid frequency as a function of the rotational speed: a) AA7075-T6 and b) AA6082-T6.

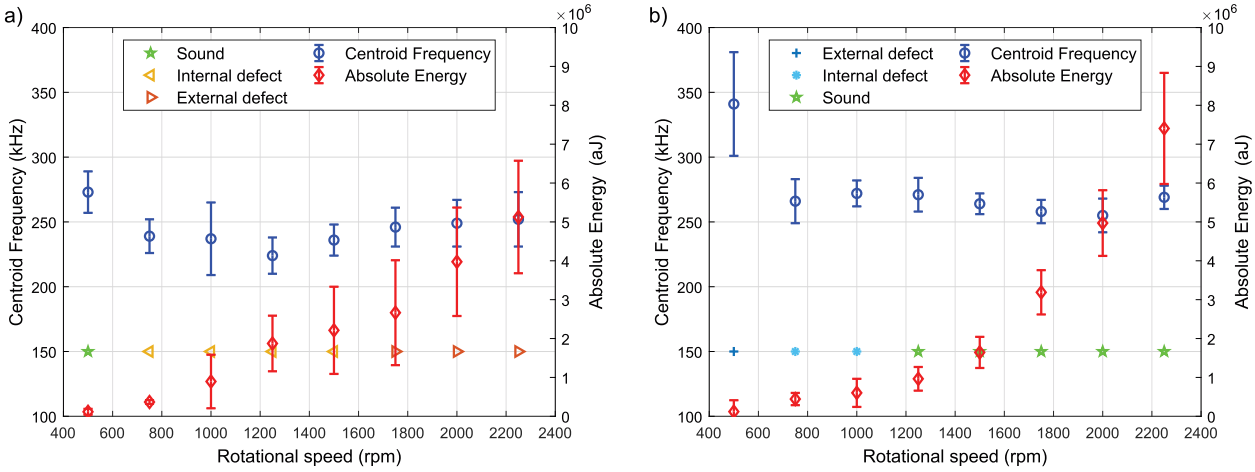

Fig. 19. Evolution of centroid frequencies and absolute energies as a function of the rotational speed in bead-on-plate tests: a) AA7075-T6 and b) AA6082-T6.

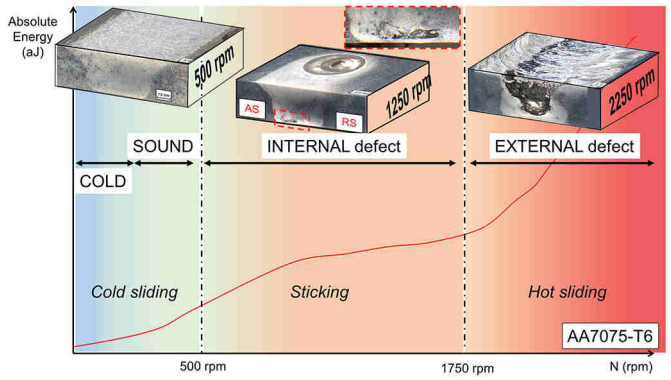

Fig. 20. Welds quality evolution for AA7075-T6 as a function of the rotational speed following the earlier introduced classification based on the absolute energy trend.

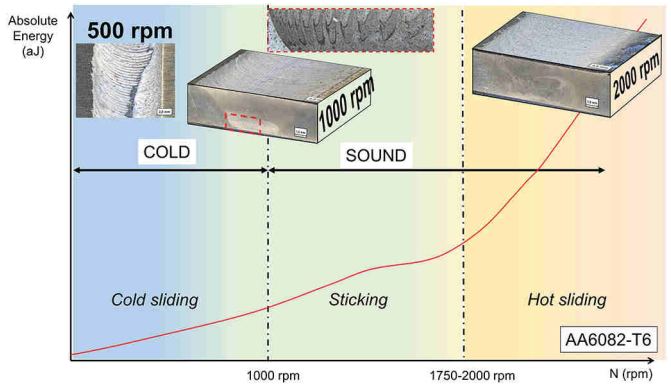

Fig. 21. Welds quality evolution for AA6082-T6 as a function of the rotational speed following the earlier introduced classification based on the absolute energy trend.

750 and 1000 rpm.

In general, in friction stir welding, various sources of acoustic emission associated with thermomechanical phenomena could be identified. On the one hand, thermal phenomena, as microstructural transformations at high temperatures and thermal expansion of the plates, generate elastic waves. However, these AE thermal sources contributions should be similar in the tests considering the high temperatures reached already at 500 rpm for both materials [20]. On the other hand, plastic deformation during the stirring forms a higher energetic acoustic emission source as it is a major degradation mechanism in the interface with relatively large material displacement. This mechanism is not a steady phenomenon among the tests and, as seen from the static tests, varies with the contact configurations and conditions. The defect appearance and the centroid frequency shift seem to result from a rheology change at the interface. In this way, a shift in AE frequency should be taken as an indicator of defective joints.

In conclusion, hot internal defects were found to be correlated with a shift in the centroid frequency below 250 kHz, while no features in AE signals correlated with the occurrence of internal cold microdefects.

4. Conclusion

This work confirmed acoustic emission measurement's potential to reveal tool-workpiece contact information and identify internal defects. The absolute energy and centroid frequency evolutions as a function of the rotational speed explained the different types of contact that can be predominantly sliding or sticking depending on the range of rotational speeds and the aluminum alloy. The transitions were corroborated by analyzing the surfaces left by the tool, energy per rotation and cross-section microstructure. Concerning the sensors' position, it was shown how it is marginal in dynamic tests, with energy and frequency differences in the elastic waves generated by the process being negligible. Therefore, for the application of acoustic emission in friction stir welding, the sensor can be fixed on the support rather than on the welding plate. In addition, when studying the attenuation of signals, another identified aspect was the influence of material viscosity variations around the tool on AE features, which depend on its chemical composition and the combination of temperature and shearing rate. Although it may seem purely phenomenological, this aspect is important because it is essential in the weldability and the range of process parameters in which sound joints can be obtained and undoubtedly requires further investigations into the rheological behavior of the two aluminum alloys under FSW conditions. Finally, the mean centroid frequency was identified as a characteristic of acoustic emissions capable of identifying internal defects induced by hot welding conditions associated with the exceedance of the solidus temperature and the consequent local incipient melting. In tests performed on the two heat-treatable alloys, AA6082-T6 and AA7075-T6, healthy joints corresponded to average centroid frequencies above 250 kHz. In contrast, when internal defects occurred at rotational speeds greater than or equal to 750 rpm for AA7075-T6, a net shift in centroid frequencies below 250 kHz was observed. The possibility of identifying a type of internal defect by monitoring acoustic emissions has been confirmed.

CRediT authorship contribution statement

Danilo Ambrosio: Conceptualization, Methodology, Validation, Formal analysis, Investigation, Data curation, Writing - Original draft, Writing - Review and editing, Visualization. **Gilles Dessein**: Formal analysis, Investigation, Writing - Review and editing, Resources, Supervision, Project administration. **Vincent Wagner**: Formal analysis, Investigation, Writing - Review and editing. **Malik Yahiaouil**: Formal analysis, Investigation, Writing - Review and editing. **Jean-Yves Paris**: Formal analysis, Writing - Review and editing. **Marina Fazzini**: Writing - Review and editing. **Olivier Cahuc**: Resources, Writing - Review and editing, Supervision, Project administration, Funding acquisition.

Declaration of competing interest

The authors declare that they have no known competing financial interests or personal relationships that could have appeared to influence the work reported in this paper.

Acknowledgement

The authors want to thank Jérémie Bega (Arts et Métiers ParisTech) for the help during the metallographic preparation and etching of the samples.

Funding

This project received funding from the European Union's H2020 Marie Skłodowska-Curie Actions (MSCA) Innovative Training Networks (ITN) H2020-MSCA-ITN-2017 under the grant agreement no 764979.

Data availability

The raw/processed data required to reproduce these findings cannot be shared at this time due to technical or time limitations.

References

[1] Tönshoff HK, Jung M, Männel S, Rietz W. Using acoustic emission signals for monitoring of production processes. Ultrasonics 2000;37(10):681–6.
[2] ASTM. E610 - Standard Definitions of Terms Relating to Acoustic Emission. pp 578–581.
[3] Kwong J, Axinte DA, Withers PJ, Hardy MC. Minor cutting edge-workpiece interactions in drilling of an advanced nickel-based superalloy. Int. J. Mach. Tools Manuf. 2009;49(7–8):645–58.
[4] Scala CM, Mc S, Cousland K. Acoustic emission during fatigue crack propagation in the aluminium alloys 2024 and 2124. Mater. Sci. Eng. 1983;61(3):211–8.
[5] Skare T, Krantz F. Wear and frictional behaviour of high strength steel in stamping monitored by acoustic emission technique. Wear 2003;255(7–12):1471–9.
[6] Godin Nathalie, Reynaud Pascal, Fantozzi Gilbert. Challenges and limitations in the identification of acoustic emission signature of damage mechanisms in composites materials. Appl. Sci. (Switzerland) 2018;8(8).
[7] Dornfeld D. Application of acoustic emission techniques in manufacturing. NDT E Int. 1992;25(6):259–69.
[8] Li Xiaoli. A brief review : acoustic emission method for tool wear monitoring during turning. Int. J. Mach. Tools Manuf. 2002;42:157–65.
[9] Jayakumar T, Mukhopadhyay CK, Venugopal S, Mannan SL, Raj Baldev. A review of the application of acoustic emission techniques for monitoring forming and grinding processes. J. Mater. Process. Technol. 2005;159(1):48–61.
[10] Behrens Bernd Arno, Hubner Sven, Wolki Kai. Acoustic emission–a promising and challenging technique for process monitoring in sheet metal forming. J. Manuf. Process. 2017;29:281–8.
[11] Chen Changming, Kovacevic Radovan, Jandgric Dragana. Wavelet transform analysis of acoustic emission in monitoring friction stir welding of 6061 aluminum. Int. J. Mach. Tools Manuf. 2003;43(13):1383–90.
[12] Zeng WM, Wu HL, Zhang J. Effect of tool wear on microstructure, mechanical properties and acoustic emission of friction stir welded 6061 Al alloy. Acta Metall. Sin. (Eng. Lett.) 2006;19(1):9–19.
[13] Soundararajan V, Atharifar H, Kovacevic R. Monitoring and processing the acoustic emission signals from the friction-stir-welding process. Proc. Inst. Mech. Eng. B J. Eng. Manuf. 2006;220(10):1673–85.
[14] Subramaniam Senthilkumar, Narayanan S, Denis Ashok S. Acoustic emission-based monitoring approach for friction stir welding of aluminum alloy AA6063-T6 with different tool pin profiles. Proc. Inst. Mech. Eng. B J. Eng. Manuf. 2013;227(3):407–16.
[15] Rajashekar R, Rajaprakash BM. Development of a model for friction stir weld quality assessment using machine vision and acoustic emission techniques. J. Mater. Process. Technol. 2016;229:265–74.
[16] Daniel FO, Braga LMC De Sousa, Infante V, Silva Lucas FM, Moreira P, Braga Daniel FO, et al. Aluminium friction-stir weld-bonded joints. J. Adhes. 2016;92(07–09):665–78.
[17] Silva-Magalhães A, De Backer J, Martin J, Bolmsjö G. In-situ temperature measurement in friction stir welding of thick section aluminium alloys. J. Manuf. Process. 2019;39(February):12–7.
[18] Handbook ASM. Properties and Selection: Nonferrous Alloys and Special-purpose Materials, Volume 2vol. 2; 1990.
[19] Aval Hamed Jamshidi. Microstructure and residual stress distributions in friction stir welding of dissimilar aluminium alloys. Mater. Des. 2015;87:405–13.
[20] Ambrosio Danilo, Wagner Vincent, Dessein Gilles, Paris Jean Yves, Jlaiel Khouloud, Cahuc Olivier. Plastic behavior-dependent weldability of heat-treatable aluminum alloys in friction stir welding. Int. J. Adv. Manuf. Technol. 2021;117:635–52.
[21] Yahiaoui M, Chabert F, Paris JY, Nassiet V, Denape J. Friction, acoustic emission, and wear mechanisms of a PEKK polymer. Tribol. Int. 2019;132(December 2018):154–64.
[22] Zaeh MF, Gebhard P. Dynamical behaviour of machine tools during friction stir welding. Prod. Eng. 2010;4(6):615–24.
[23] Morisada Y, Imaizumi T, Fujii H. Clarification of material flow and defect formation during friction stir welding. Sci. Technol. Weld. Join. 2015;20(2):130–7.
[24] Rabinowicz Ernest. Stick and slip. Sci. Am. May 1956;194(5):109–19.
[25] Gerlich A, Avramovic-Cingara G, North TH. Stir zone microstructure and strain rate during Al 7075-T6 friction stir spot welding. Metall. Mater. Trans. A Phys. Metall. Mater. Sci. 2006;37(9):2773–86.
[26] Gerlich A, Su P, Yamamoto M, North TH, Gerlich A, Su P, et al. Material flow and intermixing during dissimilar friction stir welding 2013;1718.
[27] Leitao C, Louro R, Rodrigues DM. Analysis of high temperature plastic behaviour and its relation with weldability in friction stir welding for aluminium alloys AA5083-H111 and AA6082-T6. Mater. Des. 2012;37:402–9.
[28] Souto Ulisses Borges, da Silva Rodrigo Henriques Lopes, dos Santos André Luis Beloni, da Silva Márcio Bacci. Influence of the Sensor Position in the Signal of Acoustic Emission When Monitoring Milling Operation. 2007.
[29] Maji AK, Satpathi D, Kratochvil T. Acoustic emission source location using lamb wave modes. J. Eng. Mech. 1997;123(2):154–61.
[30] Gobran NK, Youssef H. Viscous ultrasonic attenuation in metals. J. Appl. Phys. 1967;38(8):3291–3.
[31] Franke Daniel J, Morrow Justin D, Zinn Michael R, Duffie Neil A, Frank E. Experimental determination of the effective viscosity of plasticized aluminum alloy 6061-T6 during friction stir welding. Procedia Manuf. 2017;10:218–31.
[32] Kim WY, Kang CG, Lee SM, Kim WY, Kang CG, Lee SM. Effect of viscosity on microstructure characteristic in rheological behaviour of wrought aluminium alloys by compression and stirring process. Mater. Sci. Technol. 2013;0836:19–30.
[33] Zakharov VV. Scientific aspects of deformability of aluminum alloys during extrusion. Adv. Perform. Mater. 1995;2(1):51–65.